



LAWRENCE
LIVERMORE
NATIONAL
LABORATORY

UCRL-JRNL-217367

High Energy K(alpha) Radiography Using High-intensity, Short-pulse Lasers

H.-S. Park, N. Izumi, M. H. Key, J. A. King, J. A. Koch, O. L. Landen, P. K. Patel, D. F. Price, B. A. Remington, H. F. Robey, R. A. Snavely, M. Tabak, R. P. J. Town, J. E. Wickersham, C. Stoeckl, M. Storm, W. Theobald, D. M. Chambers, R. Egelton, T. Goldsack, R. J. Clarke, R. Heathcote, E. Giraldez, A. Nikroo, D. A. Steinman, R. B. Stephens, B. B. Zhang

November 29, 2005

Physics of Plasmas

Disclaimer

This document was prepared as an account of work sponsored by an agency of the United States Government. Neither the United States Government nor the University of California nor any of their employees, makes any warranty, express or implied, or assumes any legal liability or responsibility for the accuracy, completeness, or usefulness of any information, apparatus, product, or process disclosed, or represents that its use would not infringe privately owned rights. Reference herein to any specific commercial product, process, or service by trade name, trademark, manufacturer, or otherwise, does not necessarily constitute or imply its endorsement, recommendation, or favoring by the United States Government or the University of California. The views and opinions of authors expressed herein do not necessarily state or reflect those of the United States Government or the University of California, and shall not be used for advertising or product endorsement purposes.

High Energy K α Radiography Using High-intensity, Short-pulse Lasers

H.-S. Park, N. Izumi, M. H. Key, J. A. King, J. A. Koch, O. L. Landen, P. K. Patel, D. F. Price,
B.A. Remington, H. F. Robey, R. A. Snavely, M. Tabak, R. P. J. Town, J. E. Wickersham
LLNL, Livermore, CA, USA

C. Stoeckl, M. Storm, W. Theobald
LLE, Rochester, NY, USA

D. M. Chambers, R. Eagleton, T. Goldsack
AWE, Aldermaston, Reading, RG7 4PR, UK

R. J. Clarke, R. Heathcote
CCLRC/RAL, Chilton, Didcot, OX11 0QX, UK

E. Giraldez, A. Nikroo, D. A. Steinman, R. B. Stephens
GA, San Diego, CA, USA

B. B. Zhang
UC Davis, Davis, CA, USA

Abstract

We have performed experiments using Callisto, the Vulcan 100 TW and the Vulcan Petawatt high intensity lasers to understand the characteristics of high energy, K α x-ray sources and to implement workable radiography solutions at 20-100 keV. Our measurements show that the K α size from a simple foil target is larger than 60 μm , far larger than the experiment resolution requirement. The total K α yield is independent of target thicknesses verifying that refluxing plays a major role in photon generation. Smaller radiating volumes emit brighter K α radiation. 1-D radiography experiments using small-edge-on foils resolved 10 μm features with high contrast. We tested a variety of small volume 2-D point sources such as cones, wires, and embedded wires, measuring photon yields and comparing our measurements with predictions from hybrid-PIC LSP simulations. In addition to high-energy, high-resolution backlighters, future experiments will also need imaging detectors and diagnostic tools that are workable in the 20-100 keV energy range. An initial look at some of these detector issues is also presented.

1. Introduction

Many high energy density (HED) facilities utilize x-ray backlighters to diagnose and image the evolution of planar, convergent, and other more complex geometry hydrodynamic experiments. To date, these backlighters have $E_x < 9$ keV, as they are emitted by thermal plasmas created with long-pulse lasers. In the future, experiments at new facilities such as Omega-EP, ZR, and NIF will have larger and denser targets, which will require x-ray probes with 20-100 keV x-rays (and perhaps up to 1 MeV) and need better than 10 μm spatial resolution. High-energy $K\alpha$ x-ray sources can be created through energetic electron interactions in the target material after irradiation by high-intensity, short-pulse lasers with intensities $I_L > 10^{17}$ W/cm².

In this work we present high resolution high energy radiography results with >20 keV x-rays generated from high-energy, high-intensity, short pulse lasers. The paper is organized as follows: In section 2, we describe how these experiments were motivated by the radiography requirements for the next generation high energy density (HED) experiments. Section 3 describes the experimental set-up. Section 4 describes experimental results on the high energy $K\alpha$ conversion efficiencies as function of various laser parameters and compares the results to model calculations; Section 5 describes the application to 1D and 2 D radiography and Section 6 summarizes the paper

2. Motivation and Radiographic Requirements

Time-resolved radiography is an essential diagnostic capability in many HED experiments. We take as an example a material strength experiment that measures the Rayleigh-Taylor

instability growth rate in an Al sample using a 4.3 keV backlighter to derive material strength parameters under high pressure [Lorenz05, Remington04] A second example is a study of hydrodynamic jets where induced symmetric and asymmetric jets and turbulence under hydrodynamic condition are radiographed using a 4.7 keV backlighter to obtain the density evolution. [Blue05; Foster05] A third example involves radiography of imploding capsules. The instability between 2 different materials is imaged using a 6.175 keV crystal monochromatic imaging system at the Z facility. [Sinars04] The 1-9 keV backlighters used in these experiments is a proven and well-established application of the thermal emission of plasmas created by long-pulse lasers.

Future experiments on new facilities such as NIF, [Hogan01], however, will have larger, denser, and higher-Z targets than previously fielded. These will require x-ray probes with 20-100 keV x rays and possibly up to 1 MeV. Such research includes the study of material strength [Remington06] and EOS under high pressure [Celliers04, Koenig04], mid to high Z capsule implosion experiments [Dittrich99], and studies of high pR cores for double-shell ignition experiments [Amendt05]. The requirements on the probing x-ray photon energy, spatial resolution and signal to noise ratio needed to yield quantitative measurements from the radiographic images are derived from the planned HED experiments for NIF. The x-ray photon energy requirement depends on the target density, thickness, and Z, and typically corresponds to a total optical depth of about one mean free path. The spatial resolution requirement comes from the feature sizes that need to be resolved. If we apply a point projection radiography technique, we will need the effective x-ray spot size smaller than the desired spatial resolution. The signal to noise ratio requirement comes from the need to obtain an observable contrast between features of different thicknesses. In most of the HED experiments, we need to differentiate small features

on top of a thick substrate. An example of features needing to be diagnosed could be Rayleigh-Taylor induced growth of capsule surface imperfections. In order to probe the thick substrate layer, we need high flux; in order to differentiate the small thickness variation, we will need a high signal to noise ratio for the lowest transmitting object in the image.

Before we develop practical radiography techniques, we need to understand the high energy x-ray source characteristics from the laser-plasma interactions: the mechanism of the high-energy x-ray photon generation, the x-ray spot size, the conversion efficiency from laser energy to x-ray photon energy, the angular distribution, and the background spectrum. We will also need the capability for comprehensive simulations to understand the underlying physics in these processes and to scale to the higher energy petawatt lasers planned for Omega-EP, Z-Petawatt, and NIF-ARC.

The $K\alpha$ emission mechanism using high intensity lasers is a promising way of creating 20-100 keV high energy photons. As depicted in Fig 1 when a laser with intensity $>10^{17}$ W/cm² strikes a target, a forward directed “spray” of energetic electrons is created, with energies as high as ~ 100 MeV. [Key98]. This forward current draws a return current, and a very strong azimuthal magnetic field is created, with strengths predicted to be 10-100 MG or higher, as illustrated schematically in Fig. 1. As these energetic electrons traverse the target, bound electrons can be knocked out by electron-electron scattering. If a K-shell electron is knocked out, this inner shell vacancy is quickly filled by an L-shell or M-shell electron, generating isotropic $K\alpha$ or $K\beta$ radiation. This monoenergetic line radiation sits on top of a smooth Brehmsstrahlung background. For mid-to-high Z elements, these $K\alpha$ x-rays can have energies of 20-100 keV, making them ideally suited for high energy radiography. Indeed researchers in the medical community have developed techniques for coronary angiography using x-rays from lasers with 100 fs to 5 ps

pulse duration [Anderson01, Toth05] However, the laser energies for these applications are typically ~ 10 mJ yielding relatively few x-ray photons per pulse. This quantity is not enough to do single-shot radiographic imaging; the medical community uses multiple pulses to accumulate enough photons per resolution element. In addition, the required spatial resolution for medical imaging is modest ($100 - 500 \mu\text{m}$.) For our HED experiments, we need to radiograph a dynamically evolving object in a single shot, which requires a high-energy, high-intensity, short-pulse lasers.

3. Experimental Set-Up

In order to understand the $K\alpha$ source characteristics and to test high energy radiography concepts, we performed several experiments using short pulse high intensity lasers at the Callisto laser at LLNL and the Vulcan 100 TW and Vulcan Petawatt lasers at Rutherford Appleton Laboratory, UK. The Vulcan petawatt laser energy was varied between 100 to 400 J with pulse duration between 0.4 ps to 70 ps. The spot size diameter (defined to contain 50% of the laser energy) was varied between $7 \mu\text{m}$ at best focus to $42 \mu\text{m}$ by moving the target $300 \mu\text{m}$ towards the focusing parabola. We fielded imaging detectors and spectrometers to measure the high energy x-ray spot sizes and x-ray spectra, and to radiograph test targets. Specifically, we employed single photon counting camera, a crystal $K\alpha$ imager, a HOPG spectrometer, and CsI/CCD or Imaging Plate detectors to measure the absolute $K\alpha$ yields and the x-ray source size.

3.1 Single Photon Counting Camera

The use of a low-noise CCD camera as an x-ray spectrometer is a well established technique [Nishiuchi99] where the x-ray photon hits are captured in a single or a few adjacent pixels and

the total deposited intensity is proportional to the incoming x-ray photon energy. For a CCD camera, the bandgap of the Si material is 3.65 eV; a 1 keV x-ray photon, if absorbed completely in one pixel, will produce 274 photoelectrons (pe). For scientific-grade CCD cameras, a typical digitization level is ~ 1 pe per digitization level (ADU) and the noise is < 10 pe enabling us to detect multiple keV x-rays with ease. In this operation, the x-ray hits should be sparse on the CCD so that individual photon hits are well resolved and not overlapping with neighboring x-ray hits. For this experiment we employed a commercial CCD camera, SI-800, manufactured by Spectral Instruments, AZ. We have calibrated the single photon detection efficiency using radioactive Fe55 and Cd109 sources. The dominant radiation from the Fe55 isotope is 5.9 keV Mn $K\alpha$ x-rays, and from the Cd109 source 22.0 keV Ag $K\alpha$ x-rays. The absolute x-ray level is measured with calibrated silicon and CdTe detectors from Amptek using a multichannel analyzer, allowing the detection efficiency of our diagnostics to be determined. After thus calibrating our diagnostics, we are able to determine the absolute conversion efficiencies in our $K\alpha$ experiments.

3.2 Cu $K\alpha$ Crystal Imager

The Cu $K\alpha$ crystal imager utilizes a spherically-bent RAP crystal to selectively diffract and focus x-rays at the Cu $K\alpha$ energy of 8.0 keV ± 0.056 eV onto a back-thinned and cooled CCD camera. The Cu $K\alpha$ imaging diagnostic consists of a RAP crystal optic spherically bent to a radius of 38 cm and cut with the reflecting surface parallel to the 2131 plane. The crystal was positioned to Bragg reflect at second order and image Cu $K\alpha$ radiation from the target at TCC onto a Princeton Instruments, 1 square inch, 1024 x 1024 pixel internally cooled CCD. The second order Bragg reflection of 8.0 keV Cu $K\alpha$ from the 2131 planes of spacing $2d = 3.08\text{\AA}$

required a Bragg angle of 88.7° . An object distance of 20.1 cm and an image distance of 350.4 cm resulted in a magnification of 17.4. A 25 μm thick Cu foil (with the cold K-edge at 8.9 keV) placed at the CCD was used as a K-edge filter to selectively pass the 8.0 keV Cu $K\alpha$ radiation (with mean free path length of $\sim 22 \mu\text{m}$), but filter out higher energy x-rays. To minimize optical aberrations while maintaining a reasonable collection angle, the crystal was apertured to a diameter of 16mm. Astigmatism and spherical aberration limited spatial resolution to $\sim 10 \mu\text{m}$. With the given magnification, the 1 square inch CCD provided a field of view of $\sim 1.4 \text{ mm}$ at the target. The geometry of this imaging system [Koch03] is such that the point source from the laser interaction is placed on the Rowland circle and the imaging device is placed to yield a magnification of 17.4. The crystal imager was oriented at 26° off the axis defined by the laser incidence direction. When we interpret the data, we correct for the viewing angle. This diagnostic has a narrow spectral band pass, tuned to the cold $K\alpha$ line. This discriminates against contamination from other energies, but also means that if there are $K\alpha$ line shifts due to significant target heating, the $K\alpha$ emission may move outside the band pass of the imager and not be recorded. The relative brightness of different target geometries is measured as well.

3.3 HOPG Spectrometer:

The Cu $K\alpha$ radiation is also spectrally resolved with a high efficiency, sagittally curved highly oriented pyrolytic graphite (HOPG) crystal [Pak04] coupled to an image plate detector. The crystal collects x-rays emitted from the back surface at 42 degrees from the foil normal. Because of the detector's close proximity to the target center (10 cm from the center) and the fine crystal spacing, this detector has a higher sensitivity and higher spectral resolution compared

to the single photon counting camera. We used it to measure the relative brightness of targets with small $K\alpha$ yields.

3.4 Imaging Detector

We utilized two different types of imaging detectors: CsI/CCD cameras and Imaging Plates. We use a commercially available x-ray scintillator from Hamamatsu consisting of columnar grown Thallium doped CsI crystal on a fiber optic plate to convert incoming high-energy x-rays into visible photons. We glued this x-ray scintillator to an EEV 2k x 2k CCD camera. We tested the spatial resolution of this camera using the Cd109 radioactive source and measured the contrast to be better than 50% at 9 line pairs per mm (corresponding to 55 μm resolution) [Wickersham04.] We also use non-electronic imaging devices, Image Plates [Amemiya97], that are commonly used for medical imaging. A Ditabis scanner is used to scan and digitize the Image Plate data. The CsI/CCD camera is an electronic imaging device, more sensitive, reliable, and reproducible but subject to radiation backgrounds. The image plate, by comparison, is more radiation hardened and has higher dynamic range, but its sensitivity and reproducibility can vary depending on the scanner.

4. Experimental Results

4.1 22 keV Ag $K\alpha$ Spot Size Measurement

The required spatial resolution for many of the next-generation laser experiments is better than 10 μm . If we want to apply point projection imaging, we will need an x-ray source with effective spot size smaller than 10 μm . Most short pulse lasers have laser spot sizes smaller than 10 μm due to the use of short focal length, off-axis parabolas. We measured the spot size of the

OPCPA output for the Vulcan petawatt and the result is FWHM $\sim 7 \mu\text{m}$, as shown in Figs. 2a and 2b. We then measured the 22 keV Ag $K\alpha$ source size generated by this laser, using a pinhole camera filtered with a $50 \mu\text{m}$ Ag foil. The pinhole array was made of $500 \mu\text{m}$ thick Ta substrate and the pinholes were laser-drilled to $20 \mu\text{m}$ diameters. The result is shown in Figs 2c and 2d. Our measured high-energy x-ray spot size generated by this laser is $57 \mu\text{m}$ FWHM. The x-ray source sizes are factors of 5-10 larger than the laser spot size, due to the spreading of the relativistic electrons. As an independent check on the x-ray spot size, we recorded a point projection radiograph of a 3 mm outer diameter, $25 \mu\text{m}$ thick Au hohlraum and a knife-edge (disk). The spatial resolution inferred from these images is $\sim 60 \mu\text{m}$, as determined from the blurring of their edges [Park04.] We performed x-ray source size measurements of Ag targets with thicknesses of 25, 50 and $100 \mu\text{m}$ and laser intensities of $10^{18} - 10^{20} \text{ W/cm}^2$. We find that the source size is independent of target thickness and laser intensity.

We also measured the source size for higher energy 40 keV Sm $K\alpha$ radiation using the Callisto laser at LLNL. Direct pinhole imaging was not possible because of the high energy background transmitted through the pinhole substrate ($500 \mu\text{m}$ thick) dominated the direct pinhole throughput. Instead we analyzed point projection radiographs of a 3 mm thick Ta knife-edge. Our analysis shows that the size of the Sm x-ray source is also $\sim 60 \mu\text{m}$ [Wickersham04.]

Our measured $\sim 60 \mu\text{m}$ x-ray source size is much larger than the laser spot size ($< 10 \mu\text{m}$) suggesting that the hot electrons produced by the laser have spread outside of the region of direct laser illumination. Similar results have been observed in low energy $K\alpha$ experiments such as in Stephens et al [Stephens04] for 8.0 keV Cu $K\alpha$ and Reich et al [Reich03] for 4.5 keV Ti $K\alpha$. This spreading needs to be taken into account for high energy point projection radiography concepts, since most experiments require better than $10 \mu\text{m}$ spatial resolution.

4.2 Ag K α Conversion Efficiency Measurement

The absolute conversion efficiency from the laser energy to the K α source was measured using data from the single photon counting CCD detector. Figure 3a shows the image of x-ray hits from a laser shot with $E_L = 161\text{J}$ and 10 ps pulse duration on a 5 mm x 5 mm x 50 μm thick Ag foil. The pixel intensity is proportional to the incoming x-ray energy. For our CCD camera, the depletion layer is $\sim 16\text{ }\mu\text{m}$ thick; we were able to measure the x-ray hits up to a maximum x-ray energy of $\sim 30\text{ keV}$. Figure 3b shows the pixel intensity histogram from this image. In these large and relatively thick target materials, only inner-shell K α emissions are observed at these high energies. The thermal contribution (He_ α or Ly_ α lines) for Ag is negligible. In this figure the Ag K α and Ag K β signals are clearly distinguished. Note that the K α peak shows some asymmetry on the low energy side. When an x-ray hits the CCD array, the photoelectrons can spill over into neighboring pixels causing low pixel intensity registration. For conversion efficiency measurement, we ignore the hits that are spread more than one pixel but include the low energy tail. We do the same when calibrating the detection efficiency of our single hit algorithm. Hence, our conversion efficiency analysis is self consistent.

From the pixel intensity histogram, we subtract the background by fitting it to a polynomial (blue line) then correct for the detector efficiency, filter transmission and the solid angle. Using the detection efficiencies described in the earlier section, the conversion efficiency is then calculated by the ratio of the total emitted K α energy to the total incident laser energy. In functional form:

$$\epsilon_{conv} = E_{K\alpha}(total) / E_{laser}$$

$$E_{K\alpha}(total) = (E_{K\alpha}(measured) \cdot 4 \pi) / (\epsilon_{detector} \cdot \epsilon_{single_hit} \cdot T_{filter} \cdot \Omega_{detector})$$

where ϵ_{conv} is the conversion efficiency, $E_{K\alpha}(total)$ is the total energy in the $K\alpha$ x rays emitted into 4π , $E_{K\alpha}(measured)$ is the measured energy in $K\alpha$ x rays, $\epsilon_{detector}$ is detector quantum efficiency ϵ_{single_hit} is the probability that all 22 keV energy is captured in one pixel, T_{filter} is transmission factor through the filter materials, and $\Omega_{detector}$ is the detector solid angle. From the radioactive source calibration described in the previous section, we measure the combined efficiency $\epsilon_{detector} \times \epsilon_{single_hit}$ to be 5% for Cu $K\alpha$ and 0.3% for Ag $K\alpha$.

The largest uncertainty in this measurement comes from $\epsilon_{detector}$. The $\epsilon_{detector}$ is measured using the isotope source: we expose the detector for a specific time that provides the total number of x-ray photons. The absolute calibration of our detectors is known to only within a factor of 2; thus our absolute conversion efficiency is known to only within a factor of 2.

4.3 Dependency of $K\alpha$ Conversion Efficiency on Laser Intensity

During our experiments, we varied laser conditions such as laser energy, pulse duration, and laser focus resulting in different laser intensities. The conversion efficiency from laser energy to $K\alpha$ energy for both the Vulcan and Callisto experiments are plotted versus laser intensity in Fig. 4 as red circles. We measure the absolute conversion efficiency to be $\sim 10^{-4}$ for Ag $K\alpha$ for laser intensities above mid $\times 10^{17}$ W/cm². For comparison, we also show the results from similar $K\alpha$ measurements from the references: Yasuike01, Beg97, Warton98, Guo01, Anderson01, Rousse94, Jiang95, Tillman97, Schnurer96, Feurer01, Yu99, Eder00 and Theobald05. Different symbols represent different range of materials (diamonds: $Z=10-30$; circles: $Z=31-50$; squares: $Z=51-80$.) Note that these measurements are from different lasers (including low energy short

pulse lasers) and different diagnostic instrumentation. The large systematic differences cause the large spread in the measurements. Nevertheless, the conversion efficiency appears to slightly increase with laser intensity until $I_L \sim 10^{18} \text{ W/cm}^2$, above which it remains roughly flat.

4.4 Dependency of $K\alpha$ Conversion Efficiency on Element

We also studied the conversion efficiency as function of material type. Figure 5 shows the $K\alpha$ conversion efficiency as function of Z from our experiment and the other experiments mentioned in section 3.3. In this plot, the data points are divided into 2 categories: the measurements with laser intensities $> 10^{18} \text{ W/cm}^2$ (circles) and measurements with laser intensities $< 10^{18} \text{ W/cm}^2$ (diamonds.) The $K\alpha$ yield has no strong dependency on the element Z for these types of high intensity laser experiments. This is reasonable, given that each element considered has the same number of bound K-shell electrons (i.e., two), the same atomic number density (to within a factor of a few), and the laser generated hot electrons have energies far above the K-shell ionization potential. In other words, to this very energetic “electron beam”, all the K-shell electrons look nearly identical, independent of element. Two theoretical predictions are plotted in Figure 5. The dotted line is the prediction from the analytical model from Salzmann02 and Reich00 and the solid line is the prediction from the integrated modeling described in section 3.6 below. The measured and the predictions are different by up to a factor of 10.

4.5 Dependency of $K\alpha$ Conversion Efficiency on Foil Thickness

We also measured the Ag $K\alpha$ production efficiency as function of target foil thickness. We varied the Ag foil thicknesses from 12.5 to 100 μm . During our Vulcan petawatt run, Theobald et al [Theobald05] also measured $K\alpha$ yields varying the thickness from 1 to 30 μm . The resulting

K α yields for Ag and Cu foils are shown in Fig. 6. We find that the K α production is constant down to a 2 μm foil thickness. This is consistent with hot electron refluxing through the foil as the dominant mechanism of K α production.

4.6 Simulation

The interaction of a short-pulse laser with a solid-density target is a complex process that involves physics on different temporal and spatial scales. We have combined multiple independent simulation codes into one virtual code to perform simulations of the entire fast ignition process. To model the experiments reported here we have mainly performed simulations using the LSP code [Welch01] that we are using in our virtual code to transport relativistic electrons through dense plasmas. The LSP code employs a direct implicit particle push based on an energy-conserving electromagnetic algorithm [Friedman81]. This algorithm enables larger time steps than conventional explicit PIC codes, which operate on space and times scales given by the Debye length and plasmas frequency. In LSP, electrons can be represented as kinetic, or fluid particles. In the fluid description the electrons carry a temperature, which is advanced by a separate energy equation that greatly reduces the effect of numerical cooling. The net effect of these algorithms is to enable LSP to model larger, denser plasmas for longer simulation times than explicit PIC codes. We have recently modified the Monte-Carlo ITS [Halbleib92] kernel within LSP so that the only effect of this module is to generate photons. We have also integrated NLTE atomic physics tables from FLYCHK [Chung03] into LSP to calculate the charge state distribution, opacities and emissivities. These photons are transported through the target using DRAT to yield, for example, time- and space-integrated spectra, total photon yields, and K α

images. This enables us to directly compare the simulation output to the experimental measurements.

Figure 7 shows typical hot electron particle trajectories contained within a thin foil target [Town05]. We can clearly see the effect of refluxing brought about by the large electric fields generated at the front, back, and side of the target. Since few hot electrons escape the target the predicted $K\alpha$ yield is largely independent of target thickness. In fact, simulations predict that significantly brighter sources can be obtained by using mass limited targets.

4.7 Conversion Efficiency Analysis and Interpretation

We compare our experimental measurements with the simulations described in the previous section. The simulated conversion efficiencies for 22 keV Ag and 8.0 keV Cu $K\alpha$ radiation are up to a factor of 4 higher than the experimental data. This discrepancy may come from uncertainties in the laser prepulse condition, and the details of the laser beam spot profile where the effective laser intensity profile may be lower than assumed in the simulations.

5. Application of the $K\alpha$ source to Radiography

5.1 1-D Radiography Concept and Configuration

The x-ray spot size from illuminating a large disk foil with the laser at best focus is too large to be used for point projection radiography. The $K\alpha$ yield, however, is constant over a large range of foil thicknesses, due to electron refluxing. This raises the possibility of using a thin foil edge-on for projected imaging of 1-D features such as sinusoidal ripples or groves. The images shown in Figs. 8a and 8b were taken using the Cu $K\alpha$ crystal imager. These images show that the $K\alpha$ emission is restricted within the full density target material (as opposed to coming from

an expanding plasma plume) and the smaller target is brighter and more uniformly emitting x-rays. The target stalks were inadvertently made of Cu wire thus also emitting Cu K α radiation.

High resolution 1-D radiography can then be achieved by “line projection imaging” with a 5-10 μm thin foil, aligned edge-on, parallel with the 1-D rippled targets, as illustrated by the sketch in Fig 8c. In this configuration, the spatial resolution in the lateral direction will be determined by the thickness of the radiating foil.

5.2 40 keV 1-D Radiography Demonstration

We performed proof-of-principle laser shots to demonstrate the edge-on 1-D radiography concept. The schematic of the laser and the radiography target setup is shown in Figs. 9a and 9b. The 100 x 100 x 5 μm samarium (Sm) foils were prepared by laser cutting to the square shape and mounting on a 6 μm carbon fiber stalk, as shown in the figure. Since 1-D edge-on radiography relies on having a minimum lateral (edge-on) cross section, care had to be taken to cut the edges cleanly and to mount the foils so that they were flat. To minimize sensitivity to tilt, one would like very small foils. Finite laser pointing accuracy, however, prevents the disks from being too small. The 100 x 100 μm target size was a compromise between these two considerations. Fortunately due to the electron refluxing mechanism, the overall K α emitted flux is not sensitive to foil thickness or lateral extent, to first order. Note, the mean free path length of the Sm 40 keV K α x-rays in cold Sm is $\sim 200 \mu\text{m}$, so that x-ray re-absorption is minimal.

We fabricated special slits made of 12 μm thick Ta and Au substrates. These slits were made by laser cutting and they had 20, 40, 80 and 160 μm periods. Then, we added 35 to 37 μm thick Ta or Au substrate behind the 12 μm thick resolution slits. This is to simulate the expected optical depths of typical targets anticipated for laser experiments at NIF or other facilities. The

distance between the laser target, the Sm edge-on foil, and the resolution radiography object was set to 3~4 cm while the desired imaging magnification is a factor of 10 to 15 for optimal signal per resolution element. We used a 200 μm thick Sm foil as a filter to transmit 40 keV $\text{K}\alpha$ radiation while greatly reducing the lower energy and higher energy background creating a quasi-monochromatic transmission.

Figure 9c shows the resulting radiography image of the Ta slits with the CsI/CCD camera using the Vulcan TAW laser. The laser energies were 75 J for Ta with 10 ps pulse duration. For the 1-D radiography analysis, we summed and averaged the pixel intensity values along the slits to increase the signal-to-noise ratio. The resulting lineouts are shown in Figure 9d. All the resolutions patterns are clearly visible down to the 20 μm period slits in the CsI/CCD camera data.

Since our resolution patterns are square form rather than sinusoidal, from this lineout data we calculated the modulation transfer function (MTF) using a contrast transfer function (CTF) definition [Coltman54]. The modulation transfer function is derived by:

$$MTF(f) = \pi/4 [CTF(f) + CTF(3f/3) - CTF(5f/5) + CTF(7f/7)....]$$

Figure 10 shows the resulting MTF from different slit sizes and many different laser shot images. The spatial resolution, as quantified by the average MTF, was approximately 0.15, 0.4, 0.6, and 0.75 at $\lambda = 20, 40, 80,$ and $160 \mu\text{m}$.. Higher MTF will be achieved when we use high-energy lasers ($>2000\text{J}$ for NIF petawatt [Barty04] and Omega-EP [Bagnoud03]). The image contrast, MTF, also depends on the signal to noise ratio (SNR). By scaling the laser energy from our experiment, we expect to have at least 7 times more signal and 2.5 times higher SNR at NIF,

assuming the noise is mostly from photon statistics. In addition the angular alignment was only good to $\sim 1^\circ$ for the premounted targets in these experiments, which degrades the resolution measurements. This alignment accuracy can clearly be improved. With these improvements, we expect to be able to obtain high MTF for the NIF experiments.

5.3 Micro-volume $K\alpha$ conversion Efficiency

Extending our observation that the high energy x-ray sources can be confined within the target volume, we made many small targets with wires buried in different geometric shapes to create a small point source for 2-D radiography. The tested geometries are a 100 μm long Cu wire embedded in a flat Al substrate disk, a cone with a 200 μm long wire tip, a cone with a 1 mm long wire tip, a flag stalk, and a V-shaped Al substrate with a 100 μm long wire at the vertex in a “bookend” configuration. Examples of the Cu $K\alpha$ emissions from three of these targets is shown in Fig 11 for (a) a 30° Al cone with a 1 mm x 10 μm Cu wire, (b) a 30° Al cone with a 200 μm x 10 μm Cu wire, and (c) a plastic disk with a 20 μm diameter Cu wire stalk. From this data we see that the $K\alpha$ emission is mainly from the initial laser interaction region where the hot electrons are created, as shown in Fig. 11d. This implies that shorter wires will not degrade the total yields of $K\alpha$ photons enabling us to create a smaller localized source. We also had the HOPG spectrometer and a single photon counting camera for these targets. By combining their data sets, we measured the absolute $K\alpha$ yields (Fig 12.) While the target volume was varied from 15,700 μm^3 to 157000 μm^3 in this experiment, we observed that smaller volume targets generate brighter sources, such that the total $K\alpha$ yield per target volume is nearly constant, to within a factor of 2.

One big difference between the foil target and micro volume target is the total yield. In the foil target, the $K\alpha$ conversion efficiency (energy in $K\alpha$ x-rays over the laser energy) is $\sim 10^{-4}$. In contrast, we measure the conversion efficiency for the wire targets to be $\sim 10^{-5}$. One possible explanation for this low conversion efficiency may be due to the high Ohmic barrier created by the strong return current along the wire length direction ($>100\text{ }\mu\text{m}$ long), which limits the length of wire that sees the hot electron flux. The thin foils ($\leq 10\text{ }\mu\text{m}$), on the other hand, create their return current in the form of the refluxing hot electrons, so the effects of an Ohmic barrier are greatly reduced. [Key06]

In our first attempts at these small volume targets, the results of which are shown in Figs. 11 and 12, we have not yet optimized the coupling between the wire and the target substrate for the best contact. For the cone/wire targets, we have also not examined systematically the cone parameters, namely, opening angle, material, and thickness. We hope to do these optimization studies in the near future.

6. Conclusion

We have characterized high-energy $K\alpha$ source characteristics using the Vulcan and Callisto lasers. We find that the high energy $K\alpha$ source size is factors of 5-10 larger than the laser spot size. We find that the $K\alpha$ conversion efficiency is constant at $\sim 10^{-4}$ in the range of laser intensities between 10^{18} W/cm^2 to 10^{20} W/cm^2 and target foil thickness in the range between 2 to $100\text{ }\mu\text{m}$. We have demonstrated high-resolution 1-D radiography at 40 keV using a thin edge-on foil. No evidence for significant degradation of spatial resolution from a plasma plume was observed, that is, the $K\alpha$ emission seems localized to the high density target region. We have also conducted initial experiments with small micro-volume wire targets embedded in various

shapes of substrate material as possible sources for 2-D radiography. The conversion efficiencies for these sources were $\sim 10^{-5}$, which is a factor of 10 lower than the simple foil targets.

References

- [Amemiya97]: Y. Amemiya, Methods Enzymol. **276**, 233 (1997)
- [Amendt05]: P. A. Amendt et al., Phys. Rev. Lett. **94**, 065004 (2005)
- [Anderson01]: E. Andersson et al., J. Appl. Phys. **90**, 3048 (2001)
- [Bagnoud03]: V. Bagnoud et al., IFSA conference proceedings (2003)
- [Barty04]: C. P. J. Barty et al., Nucl. Fusion **44**, No 12, S266-S275 (2004)
- [Beg97]: F. Beg et al., Phys Plasmas **4**, 447 (1997)
- [Blue05]: B. Blue et al., Phys. Rev. Lett. **94**, 95005 (2005)
- [Celliers04]: P. M. Celliers et al., Phys. Plasmas **11**, L41 (2004)
- [Chung03]: H.-K. Chung et al., J. Quant. Spectroscopy & Radiative Transfer **81**, 107 (2003)
- [Coltman54]: J. W. Coltman, J. Optical Society of America **44**, No. 6, pp. 468-471 (1954)
- [Dittrich00]: T. R. Dittrich et al., Phys Plasmas **6**, No. 5, 2164 (1999)
- [Eder00]: D. C. Eder et al., Appl. Phys. B **70**, 211 (2000)
- [Feurer01]: Feuerer et al., Phys. Rev. E **65**, 01412 (2001)
- [Foster05]: J. Foster et al., Ap. J. Lett., in press (2005)
- [Friedman81]: A. Friedman et al., Cohen. Comment Plasma Phys. Contr. Fusion **6**, 225 (1981)
- [Guo01]: Guo et al., Rev. Sci. Instrum **72**, 41 (2001)
- [Halbleib92]: J.A. Halbleib et al., IEEE Trans. Nucl. Sci. NS-39, 1025 (1992)
- [Hogan01]: W.J. Hogan et al., Nucl. Fusion **41**, 567 (2001)
- [Jiang95]: Jiang et al., Phys Plasmas **2**, 1702 (1995)
- [Key98]: M. H. Key et al., Phys Plasmas **5**, 1996 (1998)

- [Key06]: M. H. Key et al., IFSA 2005 Proceedings (2006)
- [Koch03]: J. A. Koch et al., Rev. Sci. Instrum **74**, No 3, 2130 (2003)
- [Koenig04]: M. Koenig et al., Nucl. Fusion **44**, 5208 (2004)
- [Lorenz05]: K.T. Lorenz et al., Phys. Plasmas **12**, 056309 (2005)
- [Nishiuchi99]: M. Nishiuchi et al., Nucl. Instrum. Meth. Phys. Res. A **436**, 79 (1999)
- [Pak04]: A. Pak et al., Rev. Sci. Instrum **75**, No 10, 3747 (2004)
- [Park04]: H. S. Park et al., Rev. Sci. Instrum **75**, 4048 (2004)
- [Reich00]: Ch. Reich et al., Phys. Rev. Lett. **84**, 4846 (2000)
- [Reich03]: Ch. Reich et al., Phys. Rev. E **68**, 056408 (2003)
- [Remington04]: B. A. Remington et al., Met. Mat. Trans. A **35A**, 2587 (2004)
- [Remington06]: B. A. Remington et al., in press, proceedings, APS-SCCM (2006)
- [Rousse94]: A. Rousse et al., Phys. Rev. E **50**, 2200 (1994)
- [Salzmann02]: D. Salzmann et al., Phys. Rev. E **65**, 036403 (2002)
- [Schnurer96]: Schnurer et al., J. Appl. Phys **80**, 5604, (1996)
- [Sinars04]: D. B. Sinars et al., Rev. Sci. Instrum **75**, 3672 (2004)
- [Stephens04]: R. B. Stephens et al., Phys. Rev. E **69**, 066414, (2004)
- [Theobald05]: W. Theobald et al., private communication, Phys. Plasmas, to be submitted (2005)
- [Tillman97]: Tillman et al., Nuc. Instrum Meth. Phys. Res. A **394**, 387 (1997)
- [Toth05]: R. Toth et al., Proc. of SPIE, 591813 (2005)
- [Town05]: R. P. J. Town et al., Nucl. Inst. Meth. Phys. Res. A **544**, 61 (2005)
- [Warton98]: K. Wharton, Phys. Rev. Lett. **81**, 822 (1998)
- [Welch01]: D. R. Welch et al., Nucl. Inst. Meth. Phys. Res. A **464**, 134 (2001)
- [Wickersham04]: J. E. Wickersham et al., Rev. Sci. Instrum **75**, No 10, 4051 (2004)

[Yashike01]: K. Yasuike et al., Rev. Sci. Instrum **72**, 1236 (2001)

[Yu99]: J. Yu et al., Phys Plasmas **6**, 1318 (1999)

Figure Captions

1. Schematic of $K\alpha$ production mechanism. The high-intensity laser with $>10^{17}$ W/cm² creates superthermal to relativistic hot electrons. These hot electrons travel through the target material while producing $K\alpha$ and Bremsstrahlung photons. Because of the self-generated electric fields from the ions, the hot electrons reflux at the material boundary creating more photons. This mechanism is known to be much more efficient way of generating high energy photons (>10 keV) compared to the thermally driven He-like ion transitions.
2. Measured Ag $K\alpha$ source size. The left panel shows the laser spot size from Vulcan petawatt OPCPA output. Even though the laser spot is <10 mm FWHM, the x-ray spot size is much bigger than the laser spot size. This is due to the hot electron spreading and refluxing in the target medium.
3. Single photon counting image of x-ray hits from a laser interaction with a silver target. The intensity of each blob is proportional to the x-ray energy. The right panel is a histogram of pixel intensity from the CCD directly exposed to the x-rays generated from the laser interaction. The Ag $K\alpha$ and $K\beta$ peaks are clearly detected above the backgrounds. The absolute conversion efficiencies are derived from the hits above the background and convolving it with the detector efficiency and the solid angle. Note that the $K\alpha$ peak has the asymmetry towards low energy end. This is from the pixels that didn't capture all the photo electrons from the x-ray interactions; but some photo electrons are spilled over to the neighboring pixels.

4. $K\alpha$ conversion efficiency as function of the laser intensity. The conversion efficiency is defined to be the ratio of the total energy in $K\alpha$ photons to the laser energy. Different symbol represents different material ranges. Our experimental results from Vulcan and Callisto experiments are all for Ag $K\alpha$ ($Z=47$). The conversion efficiency is constant for the intensities $>10^{18}$ W/cm².
5. $K\alpha$ conversion efficiency as function of Z . Diamonds are the data with $I_L < 10^{18}$ W/cm² and the circles are $I_L > 10^{18}$ W/cm². The solid line represents the prediction by the LSP model and the dotted line is analytical model prediction from Saltzmann02.
6. $K\alpha$ photon yields as function of the foil thickness. Note that the total yields are constant down to 2 μ m thickness foil.
7. LSP simulation of thin foil target. The color represents the electron density and the lines are representative electron trajectories. The electrons are bounded within the target volume by the large electric fields; refluxes many times creating more $K\alpha$ photons.
8. Cu $K\alpha$ crystal image of small Cu foil illuminated by the Vulcan Petawatt laser. Small and thin foils can produce uniform and bright x-ray source confined within the target volume. We can utilize the thin foil as the high resolution 1-D source to radiograph 1-D line targets as sketched in the right panel.
9. Radiography of Ta resolution grid using 100 x 100 x 5 μ m Sm foil that generated quasi-monochromatic 40 keV source. The 20 μ m period features are clearly visible.
10. MTF measurements of many different laser shots of Ta and Au grids. All images are taken with the 100 x 100 x 5 μ m Sm foil. The laser energy was varied 75 to 300 J. We expect the MTF will improve when we use higher energy lasers such as planned in NIF and other facilities.

11. Cu $K\alpha$ crystal image of various micro volume wire targets attached to the cone or substrate geometry. Note that the $K\alpha$ emission is mainly confined near the initial laser interaction region.
12. $K\alpha$ yields of micro wire targets with various substrate geometries. We measure the absolute conversion efficiency of these targets are $\sim 10^{-5}$.

This work was performed under the auspices of the U. S. Department of Energy by University of California, Lawrence Livermore National Laboratory under contract W-7405-Eng-48.

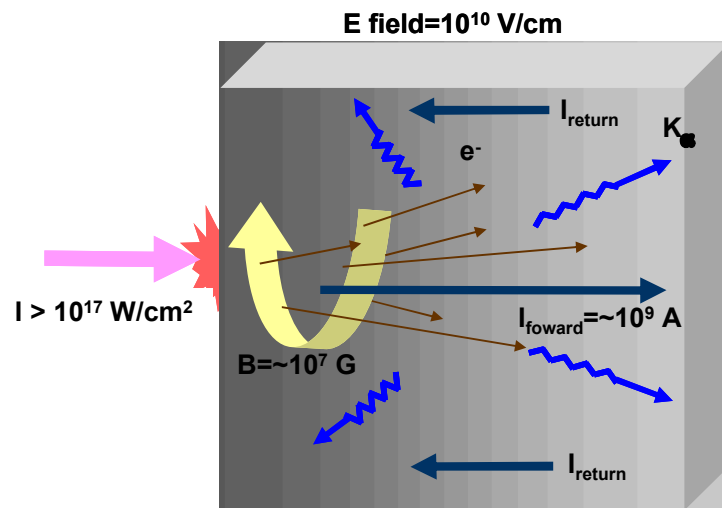


Fig 1: K^0 production mechanism

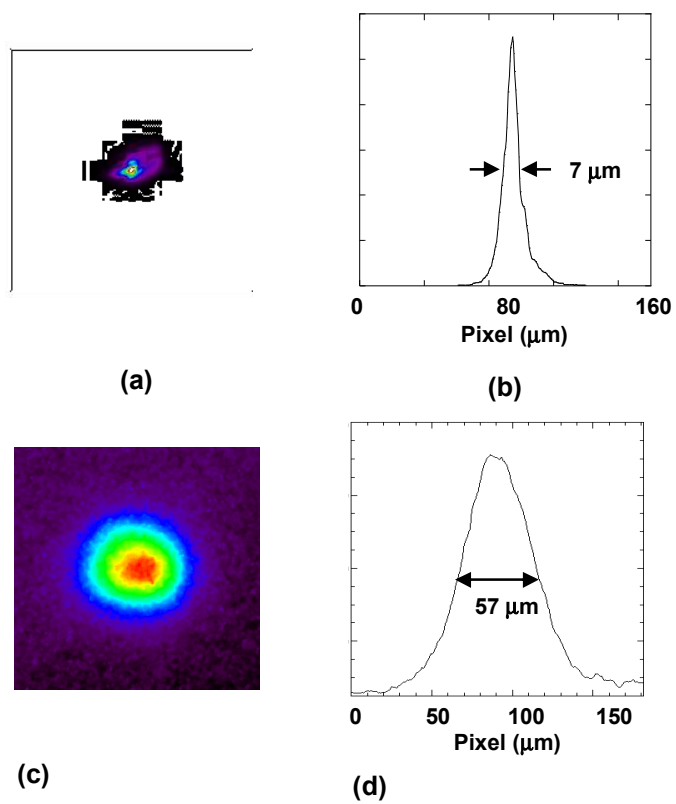
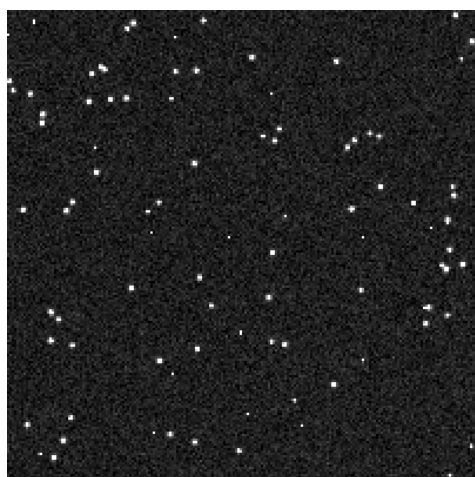
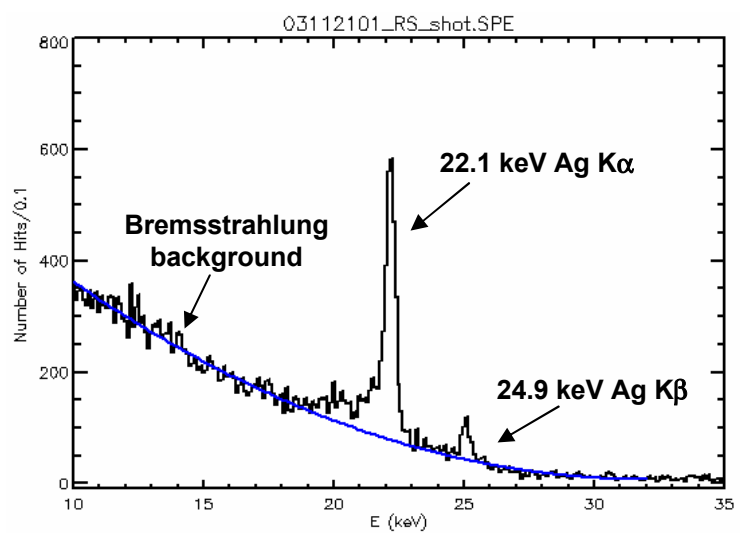


Fig 2: Ag K α source size



(a)



(b)

Fig 3: Ag $K\alpha$ single photon counting camera data



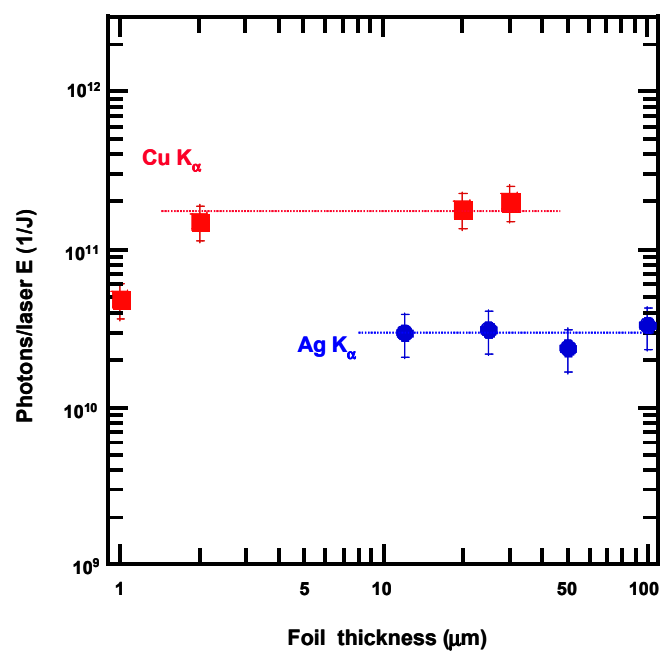


Fig 6: $\text{K}\alpha$ source foil thickness dependence

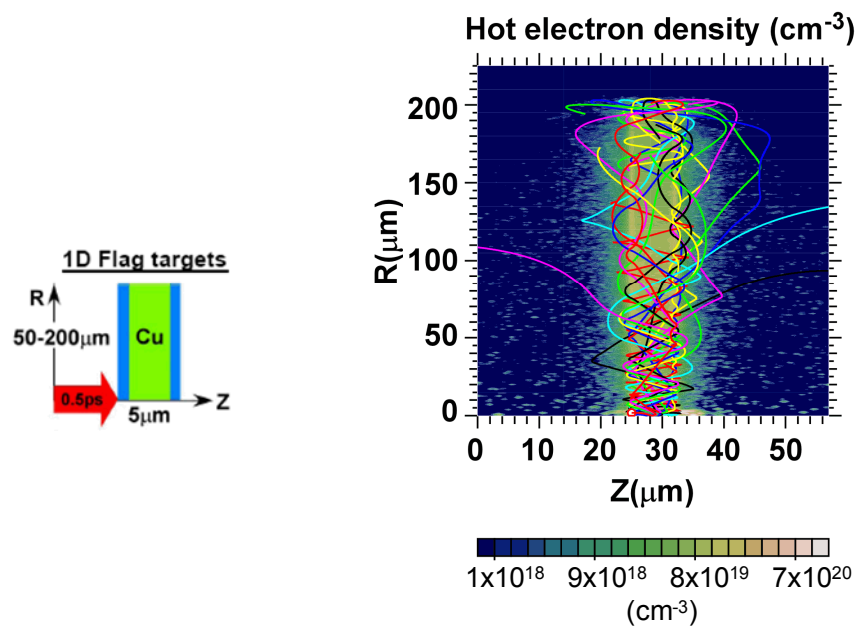
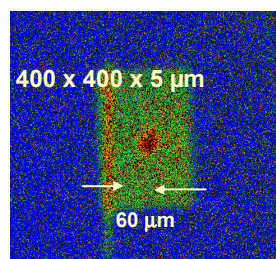
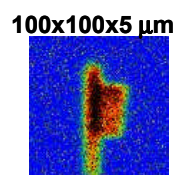


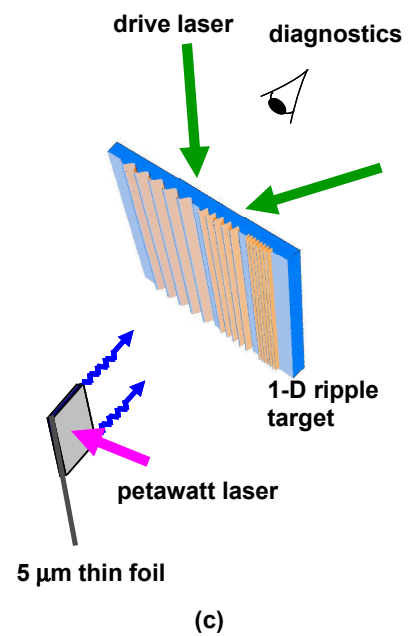
Fig 7: LSP simulation of thin foil target



(a)



(b)



(c)

Fig 8: $K\alpha$ source confinement and application to 1D radiography

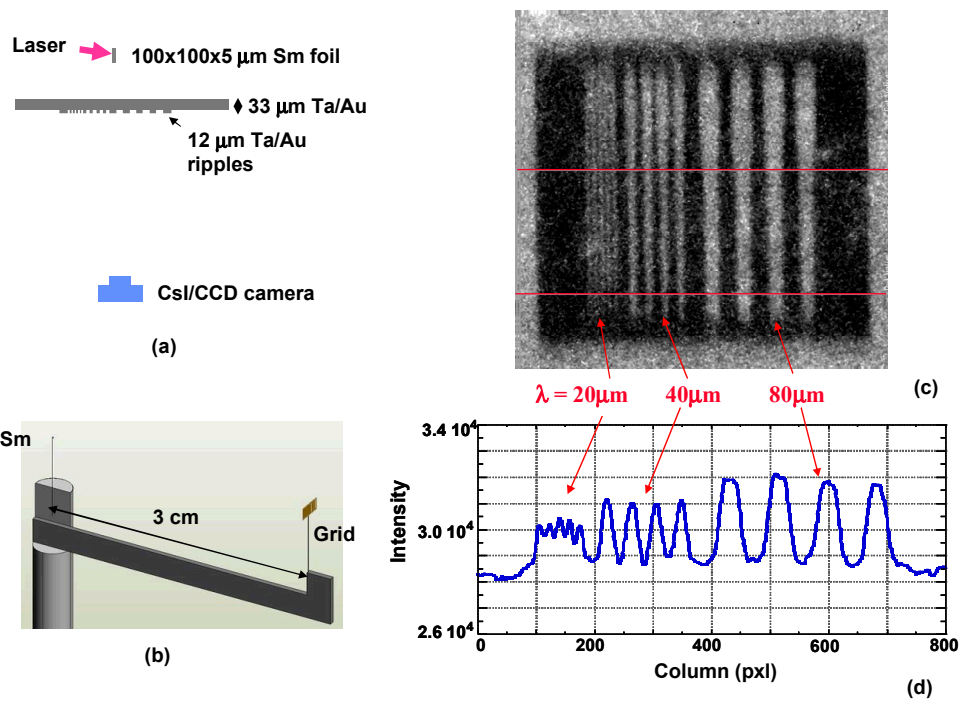


Fig 9: 1-D radiography demonstration

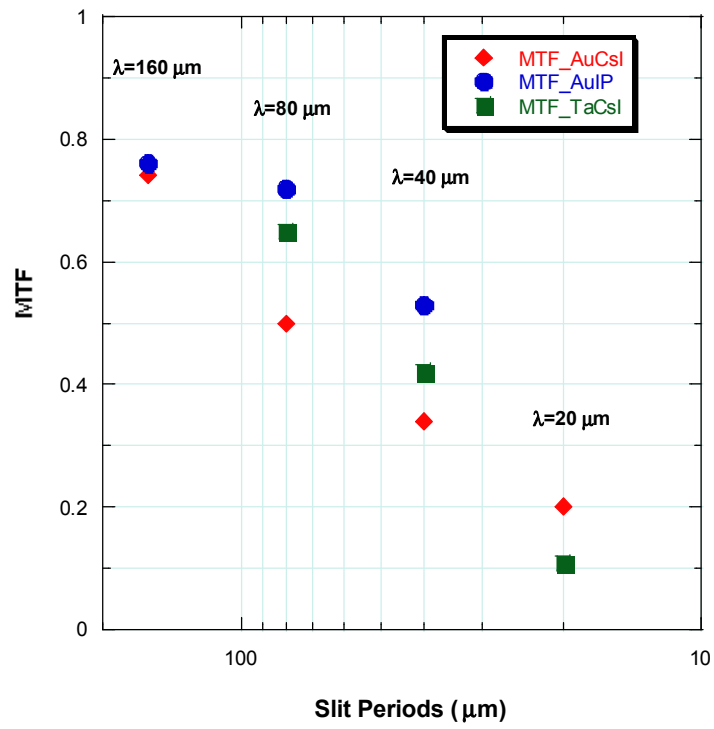


Fig 10: 1-D radiography MTF

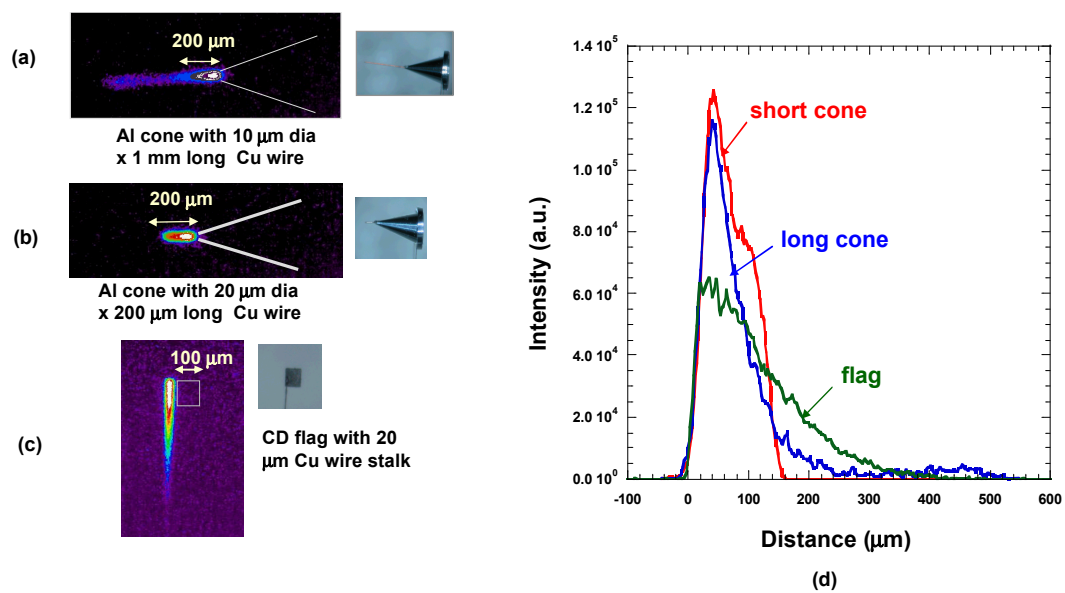


Fig 11: Cu Crystal Image of microvolume targets

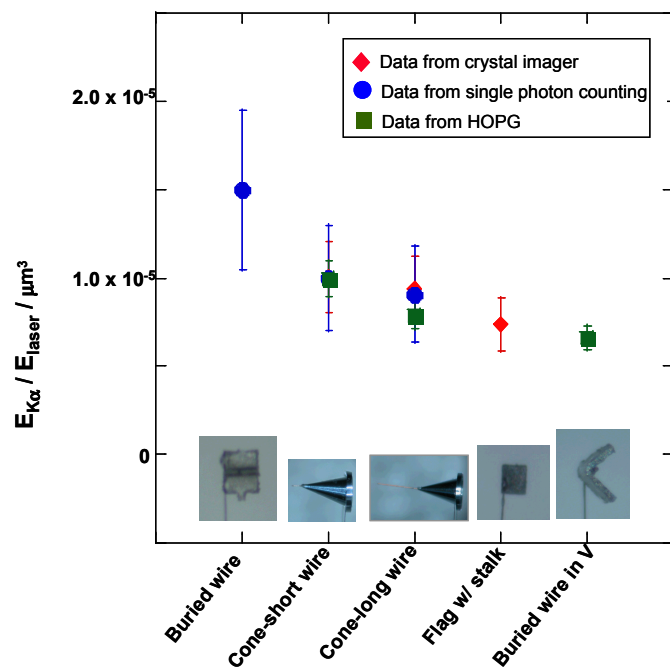


Fig 12: Micro wire volume conversion efficiency